Dalton Transactions

Experimental and Theoretical Investigation of Lithium-Ion Conductivity in Li2LaNbTiO7

Journal:	*Dalton Transactions*
Manuscript ID	DT-ART-09-2019-003547.R1
Article Type:	Paper
Date Submitted by the Author:	25-Oct-2019
Complete List of Authors:	Fanah, Selorm; University of Louisville Yu, Ming; University of Louisville, Department of Physics and Astronomy Ramezanipour, Fershid; University of Louisville, Chemistry

Experimental and Theoretical Investigation of Lithium-Ion Conductivity in $Li_2LaNbTiO_7$

Selorm Joy Fanah[1], Ming Yu[2], Farshid Ramezanipour[1,*]

[1]Department of Chemistry, University of Louisville, Louisville, KY 40292, USA

[2]Department of Physics and Astronomy, University of Louisville, Louisville, KY 40292, USA

*Email: farshid.ramezanipour@louisville.edu, Phone: +1(502) 852-7061
ORCID iD: 0000-0003-4176-1386

ABSTRACT

In line with efforts to discover new classes of lithium-conducting solids, this work utilizes density functional theory (DFT), neutron diffraction, and electrochemical impedance spectroscopy to study the lithium ion mobility in the new Ruddlesden-Popper-type oxide, $Li_2LaNbTiO_7$, where bilayer stacks of $(Nb/Ti)O_6$ octahedra are separated by layers of lithium ions. In this material, the lithium hopping distances have been shortened by incorporation of ions with smaller ionic radii, leading to a pronounced improvement in Li-ion conductivity in this family of oxides. Further enhancement of Li-ion conductivity was achieved by creation of defects in the lithium layer through the synthesis of $Li_{1.8}LaNb_{1.2}Ti_{0.8}O_7$, which contains 10% lithium-deficiency. The defects facilitate the mobility of lithium ions, leading to greater Li-ion conductivity. Detailed analysis of real and imaginary components of impedance spectroscopy and dielectric properties highlight the impact of these strategies. Neutron diffraction helps with accurate determination of lithium positions given that lithium is nearly invisible to laboratory X-ray diffraction. DFT calculations show a wide band gap, and elucidate the direction of lithium diffusion in the material lattice, as well as the energy barriers associated with Li diffusion. These calculations show that lithium diffusion occurs parallel to b and c axes of the unit cell. They also show an energy bottleneck, which is a result of close proximity of lithium and oxygen in inter-stack spaces.

Keywords: Lithium ion mobility; Materials design; Defects

1. INTRODUCTION

The study of lithium mobility in solids is essential to advances in lithium ion batteries, which are used in most portable devices.[1-3] The cycling of lithium in these batteries is responsible for their high energy density, power performance and safety, making them suitable for portable electronics, power tools, and hybrid or fully electric vehicles.[4, 5] While cathode and anode components of Li-batteries are solid, the electrolytes commonly used in these batteries are liquid. The development of solid electrolytes has long been a goal in battery industry. Therefore, further advances in battery technology, particularly in the area of solid electrolytes, requires detailed understanding of lithium diffusion through solid lattices.

Oxide materials are considered suitable candidates for this purpose, given their ability to conduct lithium ions, their tunability and stability from both chemical and mechanical standpoints.[5] A wide range of oxide materials, with different structure types, have been investigated for their lithium conducting properties. Among them, perovskites[5, 6] and garnet oxides[7, 8] have been explored extensively.

Another potentially interesting class of oxides is the Ruddlesden-poppers family, which have demonstrated remarkable properties such as ion-exchange,[9, 10] carbon dioxide capture,[11] and photocatalytic activity.[12] However, their lithium-ion conductivity has received little attention with only a handful of reports on their lithium transport,[6, 10, 13] despite their interesting structural properties that can provide useful pathways for lithium mobility. The general formula of Ruddlesden-Popper oxides can be described as $A'_2[A_{n-1}B_nO_{3n+1}]$, where corner-sharing BO_6 octahedra form bilayer, trilayer or tetralayer stacks, separated by A'-ions. The number of layers in each stack is represented by *n*, which can be as high as infinity, where the structure transforms into a perovskite. The intra-stack spaces between the BO_6 octahedra are occupied by the A-cations.

Figure 1 shows the Ruddlesden-Popper structure where $n = 2$. Given the wide separation of stacks, the inter-stack spaces might be good pathways for lithium mobility if Li can be incorporated into these spaces. Only a few $n = 2$ compounds containing Li have been reported.[11, 14-16] Among them, the lithium-ion transport in $Li_2SrTa_2O_7$ has been studied,[17] showing appreciable, but not significant conductivity. We have recently demonstrated that it is possible to enhance the Li-conductivity of this compound by incorporation of La and Ti into the composition, and creation of vacancies in the lithium layer.[18]

In the present work, we report a new Ruddlesden-Popper compound and its Li-deficient analogue, and utilize a combination of computational and experimental methods to investigate the lithium-ion conductivity. We further demonstrate the effect of defects and ionic radii on the enhancement of conductivity, and elucidate the conduction pathways of lithium ions in the material lattice.

2. EXPERIMENTAL AND COMPUTATIONAL METHODS

Synthesis. The polycrystalline compounds were prepared by solid-state method. Stoichiometric amounts of La_2O_3 (Alfa Aeasar, 99.99%), Nb_2O_5 (Alfa Aeasar, 99.993%), Li_2CO_3 (Alfa Aeasar, 99.998%), and TiO_2 (Sigma Aldrich, 99.99%) were used as starting materials. About 5% extra Li_2CO_3 was added to the starting mixture of precursors in order to compensate for Li volatility at high temperatures. The reagents were mixed in an agate mortar, pressed into cylindrical pellets and heated in alumina crucibles at 1150 ºC for 10 hrs in air. The pellets were then ground, re-pelletized and heated again under the same conditions. The heating and cooling rates in all syntheses were 100 ºC/h.

Characterization. Structural characterizations were conducted by powder X-ray diffraction at room temperature, using Cu $K\alpha_1$ radiation (λ= 1.54056Å) on an Empyrean diffractometer. Neutron

diffraction experiments were performed at room temperature using vanadium sample holder, on POWGEN beamline at Oak Ridge National Laboratory. The diffraction patterns were analyzed by Rietveld method using the program GSAS,[19] suited with EXPGUI interface. The microstructural morphology was performed using a high-resolution field-emission scanning electron microscope (SEM).

The ionic conductivity measurement of sintered pellets (~1.4 mm in thickness and ~9.0 mm in diameter) was performed in the air, using lithium-ion blocking gold electrodes. Gold paste was painted on the surface of the sample as current collector and cured at 600 ºC. The AC impedance measurements were conducted in the temperature range of 25 to 600 ºC, and frequency range of 0.1 Hz to 1 MHz. The impedance measurement was taken for each material after equilibration at a constant temperature for 1hr.

Density Functional Theory Calculations. The density functional theory (DFT)[20, 21] framework, implemented in the Vienna Ab-initio Simulation Package (VASP),[22] was used for computational calculations. The Projector Augmented Wave (PAW)[23] was utilized for the electron-ion interactions, and the generalized gradient approximation (GGA)[24] in the scheme of Perdew Burke Ernzerhof (PBE)[25] was used for treatment of electron exchange-correlation interactions. The spin polarized behavior was also taken into consideration. The Congregate-Gradient algorithm,[26] implemented in VASP, was used for structural relaxation. The energy cutoff for the plane wave basis was set at 400 eV, and the criteria for convergences of energy and force in relaxation processes were set to be 10^{-5} eV and 10^{-4} eV/Å, respectively. A primitive 1x1x1 cell was chosen and the Brillouin zones (BZ) were sampled by 5 × 5 × 5 k-point meshes created based on the Monkhorst-Pack scheme.[27]

3. RESULTS AND DISCUSSION

3.1. Crystal Structure

The crystal structure was studied using a combination of neutron and X-ray diffraction. Rietveld refinements were performed using GSAS software[19] and EXPGUI interface.[28] The bilayer Ruddlesden-Popper compounds, $A_{n+1}B_nO_{3n+1}$,[29] with n = 2, typically crystalize in tetragonal[13, 14, 30] *I4/mmm*,[16] and $P4_2/mnm$,[13] or orthorhombic *Fmmm* and *Cmcm* space groups.[15, 16, 31] For $Li_2LaNbTiO_7$, the powder X-ray diffraction peaks (Figure 2) could be readily indexed on *Cmcm* space group. The tetragonal structures were ruled out given the peak splittings at 2θ = 38.2, 58.70, 60.7, 68, 69,77.5 and 78.0º (d = 2.36, 1.57, 1.38 Å) which should be single peaks in tetragonal symmetry. Detailed structural analyses using neutron diffraction data at the low-d region revealed small peaks at *d* = 1.115 Å and 1.505 Å, which rule out the face-centering in orthorhombic symmetry, confirm the *Cmcm* space group. The use of neutron diffraction in structural analyses of this class of materials is essential. While the heavier atoms, such as La, Nb, and Ti, can be easily studied by X-ray diffraction, the investigation of lighter atoms, such as oxygen and lithium, by X-ray is more challenging. Indeed, the study of elements with very low atomic number, such as lithium, is not possible using laboratory X-ray diffraction. Whereas, such atoms can be readily investigated by neutron diffraction, as the neutron scattering lengths and cross sections are independent from atomic numbers. Figure 2b shows the Rietveld refinement profile using neutron diffraction. The structure of $Li_2LaNbTiO_7$ consists of bilayer stacks of $(NbTi)O_6$ octahedra (blue polyhedra in Figure 1), separated by lithium ions (gray spheres). The lanthanum ions (large blue spheres) occupy the available spaces within the stacks. The refined structural parameters are listed in Table 1. The lithium ions, located in inter-stack spaces, form edge-sharing LiO_4 tetrahedra, as demonstrated in Figure 1b. The tetrahedra are distorted and there are two sets of lithium-oxygen

bond lengths, Li-O1 = 2.0184 (× 2) and Li-O2 = 2.1043 (× 2). The edge-sharing tetrahedra for two-dimensional layers in the *bc* plane. As will be discussed later, the Li-mobility takes place through these layers. We postulated that creating free spaces for lithium ions within these layers can enhance the lithium-ion mobility. We therefore synthesized the lithium-deficient analogue, $Li_{1.8}LaNb_{1.2}Ti_{0.8}O_{7,}$ to study this effect. In this material, there is 10% Li-deficiency, and the charge balance is maintained by changing the Nb/Ti ratio. The defect material has the same crystal structure as the parent material, as described above (Table 2). The microstructures observed in scanning electron microscopy images (Figure S1) show a small increase in the crystallite size for the Li-deficient material.

3.2. Ionic Conductivity

The ionic conductivity was investigated by electrochemical impedance spectroscopy over a range of frequencies and temperatures. This technique offers an opportunity for the separation of the contributions that arise from the grain, grain boundary and electrode properties. When modeled in terms of equivalent electrical circuits, this technique offers an understanding of transport processes taking place in the material. [13, 32, 33] The complex impedance is expressed as $Z^* = Z' - jZ''$, where Z' and Z'' represent the real and imaginary axes of the plot respectively. These parts can be expressed as:[34]

$$Z' = \frac{R_g}{1 + (\omega R_g C_g)^2} + \frac{R_{gb}}{1 + (\omega R_{gb} C_{gb})^2} \quad , Z'' = \frac{R_g}{1 + (\omega R_g C_g)^2} + \frac{R_{gb}}{1 + (\omega R_{gb} C_{gb})^2} \qquad (1)$$

where ω = angular frequency, R_g = grain resistance, R_{gb} = grain boundary resistance, C_g = grain capacitance and C_{gb} = grain boundary capacitance. Figures 3 and 4 show typical impedance data for $Li_2LaNbTiO_7$ and $Li_{1.8}LaNb_{1.2}Ti_{0.8}O_7$ in Nyquist plots. The semicircles in these plots represent

the relaxation processes in the material, as will be discussed later. The observed spike (tail) in the low-frequency region is an indication of the blocking of mobile lithium ions at the electrode interface, a property which is commonly observed in ionic conductors.[2, 3, 5, 6, 33, 35]

The total resistance can be determined from the intercept with the real axis (Z') in Nyquist plots, as shown in Figures 3 and 4. However, it is also possible to distinguish the bulk and grain-boundary contributions to total resistance. The nature of the semicircle in impedance data can be described based on the merging of two relaxation processes, related to the bulk and grain boundary, occurring at time-scales which are not significantly different.[13, 34] In order to estimate the contribution of each, we used a resistance-capacitance (RC) model consisting of a series of two RC units, as seen in the inset of Figures 3 and 4, where R1 and R2 represent the polarization resistances for bulk and grain boundary, respectively. The CPE components represent the constant phase elements, which model the capacitance behavior in bulk (CPE1), grain-boundary (CPE2), and electrode interface (CPE3). The latter is used for modeling the observed tail in the data, corresponding to the lithium blocking at the electrode surface.[13, 32, 34] As a typical example, the fits for $Li_2LaNbTiO_7$ data at 100 °C give R1 = 3.341×10^6 Ω, CPE1 = 5.998×10^{-11} F , R2 = 1.038×10^7 Ω, CPE2 = 1.995×10^{-10} F, and CPE3 = 5.937×10^{-7} F. The CPE values are consistent with those expected for bulk, grain boundary and electrode surface polarization, which should be in the order of 10^{-11} F, 10^{-10} F, and 10^{-7} F, respectively.[13, 33, 35, 36]

The total resistance (R) obtained from the impedance data is used to calculate the conductivity (σ) using $\sigma = L/RA$, where L represents the thickness and A is the cross-sectional area of the cylindrical pellet, used for these measurements. $Li_2LaNbTiO_7$ shows detectable conductivity and a semicircle at temperatures higher than 100 °C. The lack of room temperature conductivity has been observed in the previously reported compound, $Li_2SrTa_2O_7$ as well.[6] However, when compared to

$Li_2SrTa_2O_7$,[6] our material shows higher conductivity by nearly two orders of magnitude. For $Li_2SrTa_2O_7$, the conductivity is reported at 300 ºC. Therefore, we compare the conductivities at this temperature, which are 5.0×10^{-7} S cm^{-1} for $Li_2SrTa_2O_7$[6] and 2.150×10^{-5} S cm^{-1} for $Li_2LaNbTiO_7$. The enhanced conductivity of $Li_2LaNbTiO_7$ indicates the success of our material design strategy, i.e., compressing the unit cell and shortening the Li-Li hopping distance through incorporation of ions with smaller ionic radii in the material composition. The ionic radii of La^{3+} (1.36 Å) and Ti^{4+} (0.605 Å) are smaller than those of Sr^{2+} (1.44 Å) and Ta^{5+} (0.64 Å), respectively.[37] A comparison between the two materials shows the shortening of Li-Li separation in $Li_2LaNbTiO_7$, where these distances can be as short as ~ 2.75 Å, as compared to ~ 2.80 Å for $Li_2SrTa_2O_7$.

Given our prior experience,[18] we postulated that the lithium-ion conductivity can be enhanced further if vacancies were created in the lithium layer to allow more facile mobility of lithium ions. This strategy was proven successful through the synthesis and investigation of $Li_{1.8}LaNb_{1.2}Ti_{0.8}O_7$, which showed enhanced lithium ion conductivity. The impedance data for this compound has a semicircle, and detectable conductivity at room temperature. As shown in Table 3, the Li-deficient compound shows significantly enhanced conductivity, which is several times greater than that of the parent non-deficient material. The observed trend is similar to that of the Ta-analogue, which we reported previously.[18] The increase in lithium-ion conductivity due to defects in the lithium-layer (Figure 1b) indicates that Li mobility pathways in this class of compounds are through the Li-layer in *bc* plane. This was also confirmed by density functional theory calculation, as discussed later. The increase in temperature leads to a gradual increase in conductivity, as expected, due to the enhanced mobility of lithium ions at higher temperature, eventually reaching $\sim 10^{-3}$ S cm^{-1} at 500 °C. A gradual shrinking of semicircle is observed as temperature increases, a feature which is

commonly observed in ionic conductors.[2, 3, 38, 39] It is noted that the Li-ion conductivity of these materials is still not enough for practical application. Some solid Li-ion conductors such as garnets show conductivity in the order of 10^{-4} S cm^{-1} at room temperature.[7, 8]

A plot of the temperature dependence of the conductivity of both materials based on the Arrhenius equation is shown in Figure 5. The activation energies for the thermally activated conductivities were calculated from the Arrhenius equation:[18]

$$\log\sigma T = \log\sigma_{\circ} - \left(\frac{Ea}{2.303kT}\right) \qquad (2)$$

where σ_o is a pre-exponential factor, characteristic of the material, and Ea, k and T are the activation energy, Boltzmann constant, and the absolute temperature respectively.[40, 41] The calculated activation energies were 0.676 and 0.647 eV for $Li_2LaNbTiO_7$ and $Li_{1.8}LaNb_{1.2}Ti_{0.8}O_7$, respectively. The thermal activation energies are similar, and the enhanced conductivity of $Li_{1.8}LaNb_{1.2}Ti_{0.8}O_7$ is a result of vacancies in the lithium layer.

The variation of the real part of impedance (Z') as a function of angular frequency over a range of temperatures for both compounds is shown in Figures 6. There is a decrease in Z' as the frequency increases. This is a common behavior,[34, 42-45] and could indicate the lowering of energy barriers[44] and enhanced conductivity across grain-boundary[42-44] at high frequency. Also, there is a significant decrease in Z' with temperature, consistent with the negative temperature coefficient of resistance in these materials. [42-44] Figure 7 shows the variation of the imaginary part of impedance (Z") as a function of angular frequency at different temperatures. A broad peak is observed, which eventually flattens as temperature increases, a common behavior for the imaginary part of impedance.[34, 42-44] The occurrence of this peak indicates the presence of immobile species at low temperature,[44] which become mobile as temperature increases. The disappearance of the peak and the overall decrease in the magnitude of Z'' at higher temperature

confirm the temperature dependence of relaxation phenomena.[42-44] Importantly, a comparison between the Z" peaks of $Li_2LaNbTiO_7$ and $Li_{1.8}LaNb_{1.2}Ti_{0.8}O_7$ indicates that the peak for the latter is shifted toward higher frequency, which implies an increase in the rate of hopping of localized charge carriers,[34] as expected considering that defects created in the Li-layer of $Li_{1.8}LaNb_{1.2}Ti_{0.8}O_7$ enhance the Li-ion mobility. The dielectric constant (ε') and dielectric loss (tan δ) are also calculated using the following equations:

$$\varepsilon' = \frac{t}{\omega A \varepsilon_o} \cdot \frac{-Z''}{Z'^2 + Z''^2}\ ,\ \varepsilon'' = \frac{t}{\omega A \varepsilon_o} \cdot \frac{Z'}{Z'^2 + Z''^2}\ ,\ \tan\delta = \frac{\varepsilon''}{\varepsilon'} \qquad (3)$$

where A is the cross sectional area of the sample, t is the thickness of the sample, ε_o is permittivity of free space, Z' is the real part of impedance and Z" is the imaginary part of impedance.[34, 46, 47] There are minor variations in the literature about the formula used for dielectric constant (ε'). The negative sign in the numerator is sometimes shown[46, 47] and sometimes absent.[34] Also, some researchers have represented the $t/A\varepsilon_o$ part as inverse of capacitance $1/C_o$.[46, 47]

Figure S2 shows dielectric constant (ε') and dielectric loss (tan δ) as a function of frequency at different temperatures for both compounds. There is a decrease in dielectric constant as the frequency increases, which indicates the inability of electric dipoles to conform to the fast reversal of the AC electric field at high frequency.[8, 34] This behavior is typical of ionic conducting materials.[8] At high frequencies, the oscillating charge carriers can not contribute significantly to the dielectric constant, and the dielectric properties arise from electronic polarization.[8, 43] The larger dielectric constant at low frequency arises from dipolar and interfacial polarization (i.e., Maxwell–Wagner–Sillar polarization).[8, 43] The dielectric constant values increase at higher temperature, as the mobility of thermally activated charge carriers[8] and the reorientation of dipoles is facilitated by increase in temperature.[34] Also, at higher temperatures, the plateau in the dielectric constant plot is shifted to higher frequency, indicating that the dipolar polarization is thermally activated.[8]

The dielectric loss (tan δ) occurs due to the dissipation of the electrical energy that would otherwise be used to induce polarization in the material.[34] The plot of tan δ versus frequency shows a peak, similar to that observed in other ionic conductors.[8] The peak shifts to higher frequency as temperature increases, indicating the enhancement in the mobility of charge carriers.[45] Importantly, a comparison between the dielectric loss peaks for $Li_2LaNbTiO_7$ and $Li_{1.8}LaNb_{1.2}Ti_{0.8}O_7$ shows that the peak for $Li_{1.8}LaNb_{1.2}Ti_{0.8}O_7$ appears at higher frequency, further confirming the enhanced mobility of lithium-ions in $Li_{1.8}LaNb_{1.2}Ti_{0.8}O_7$.

The complex modulus spectra (M′ versus M″) for the ion transport phenomena at different temperatures in both compounds is shown in Figure 10. The modulus analysis can be used as a tool for exploring the dynamic aspects of charge transport such as ion/carrier hopping rates and relaxation times of conductivity.[34,43,45] The electrical modulus in terms of complex modulus function can be expressed as:[34] $M^* = M' + j\,M''$

The real and imaginary components of the complex modulus can be described as: $M' = \frac{\varepsilon'}{\varepsilon'^2 + \varepsilon''^2}$ and $M'' = \frac{\varepsilon''}{\varepsilon'^2 + \varepsilon''^2}$, where ε′ and ε″ are the real and the imaginary components of dielectric permittivity, respectively.[34] The complex modulus spectra of M″ versus M′ for the parent and the lithium-deficient material are shown in Figure S3. In addition, the variation of real (M′) and imaginary (M″) parts of modulus as a function of frequency at different temperatures is shown in Figure S4. As observed from the variation of the real part as a function of frequency at selected temperatures, M′ tends to be very small, close to zero, in the lower frequency region. As frequency increases, there is an increase and dispersion in M′. The observed dispersion may be the result of short-range mobility of charge carriers. The plot patterns also show variation of M′ as a function

of temperature, which indicates the temperature-dependence of relaxation processes in these materials.[32,34,43]

The plot of M" versus frequency shows a peak, which shifts towards higher frequency as temperatures rises. This indicates the correlated motion of mobile ions[34] and once again confirms the temperature-dependence of ionic mobility. The peak frequency is indicative of a transition from long-range (below the peak) to short-range (above the peak frequency) ionic mobility.[43] The broad asymmetric shape of the peak is suggestive of a non-Debye type relaxation with different time constants.[34,43]

3.3. Density Functional Theory Calculations

The DFT calculations were utilized to examine the lithium conduction pathways in this series of compounds. The energy barrier for lithium diffusion in $Li_2LaNbTiO_7$ was investigated. The band structure and density of states were also calculated, showing a large band gap of 2.086 eV, as shown in Figure 8. The mobility of lithium ion in different directions in $Li_2LaNbTiO_7$ was examined and the energy associated with each pathway was calculated. In these calculations, lithium ions were gradually displaced from their lattice position, and the change in the energy of the system was computed at different distances in a particular direction. The lithium hopping in *x*-direction (parallel to the unit cell axis *a*) is unrealistic given the long separation (~10 Å) between lithium layers in the *a*-direction. Therefore, the energy barrier for lithium mobility in $Li_2LaNbTiO_7$ was calculated for *b* and *c*-directions. It was found that in this material, the energy barriers in both directions are identical.

Figure 9 shows the graph of diffusion energy versus lithium-displacement in the *b*-direction. The diffusion energy is defined as the energy of the system relative to the state where Li ions are in

their original position. As demonstrated in this figure, the displacement of lithium from its original position leads to an increase in the energy of the system, which reaches a peak at ~ 1.5 Å. As shown in the inset of Figure 9, the energetic bottleneck is associated with close proximity of lithium ions to oxygens located above and below the lithium layer. The close interaction of lithium and oxygen drives the energy of the system higher. The energy barrier of ~1 eV is high compared to some other ionic conductors,[48-50] where the energy bottleneck can be as small as ~0.1 eV.[50] For comparison, the diffusion energy was also calculated for $Li_{1.8}LaNb_{1.2}Ti_{0.8}O_7$ in *b*-direction. As shown in Figure 9, the diffusion energy for the Li-deficient compound follows the same trend as the parent material, reaching a peak at ~ 1.5 Å for Li displacement. There is a slight decrease in the energy barrier for the Li-deficient compound compared to the parent material.

The information obtained from DFT calculations can be helpful in designing materials with higher Li conductivity. These results show that the proximity of lithium and oxygen in the bottleneck is the main reason for the high energy barrier. Therefore, one may envision the possibility of lowering the energy barrier by increasing the separation of the octahedral stacks (Figure 1), which can lead to longer distances between oxygen and lithium ions located between the stacks. This may result in better mobility of lithium ions and lower diffusion energy.

4. CONCLUSIONS

The shortening of lithium hopping distances by incorporation of cations with smaller ionic radius in the Ruddlesden-Popper structure can lead to the enhancement of lithium-ion conductivity, as shown in $Li_2LaNbTiO_7$, compared to $Li_2SrTa_2O_7$. Furthermore, the creation of defects in the inter-stack lithium layer can enhance the conductivity further, as demonstrated through the synthesis and investigation of $Li_{1.8}LaNb_{1.2}Ti_{0.8}O_7$. The direction of lithium diffusion is parallel the unit cell

axes *b* and *c*. The energy barrier for lithium diffusion is associated with close proximity of lithium and oxygen atoms. This information may be used for future design of Li-conducting Ruddlesden-Popper oxides, where wider separation of stacks can prevent the close proximity of lithium and oxygen, leading to the lowering of energy barrier for lithium diffusion.

Conflicts of interest

The authors declare no conflict of interest.

Acknowledgements

F.R. thanks the Conn Center for Renewable Energy Research. This work is supported in part by the National Science Foundation under Cooperative Agreement No. 1355438.

References

1. R. Murugan, V. Thangadurai and W. Weppner, *Ionics*, 2007, **13**, 195-203.
2. V. Thangadurai and W. Weppner, *J. Am. Ceram. Soc.*, 2005, **88**, 411-418.
3. V. Thangadurai and W. Weppner, *Adv. Funct. Mater.*, 2005, **15**, 107-112.
4. N. Nitta, F. Wu, J. T. Lee and G. Yushin, *Materials Today*, 2015, **18**, 252-264.
5. R. Murugan, W. Weppner, P. Schmid-Beurmann and V. Thangadurai, *Mater. Res. Bull.*, 2008, **43**, 2579-2591.
6. T. Fukushima, S. Suzuki and M. Miyayama, *Key Eng. Mater.*, 2009, **388**, 69-72.
7. S. Narayanan, F. Ramezanipour and V. Thangadurai, *Inorg. Chem.*, 2015, **54**, 6968-6977.
8. A. K. Baral, S. Narayanan, F. Ramezanipour and V. Thangadurai, *Phys. Chem. Chem. Phys.*, 2014, **16**, 11356-11365.
9. J. Gopalakrishnan and V. Bhat, *Inorg. Chem.*, 1987, **26**, 4299-4301.
10. N. S. P. Bhuvanesh, M. P. Crosnier-Lopez, O. Bohnke, J. Emery and J. L. Fourquet, *Chem. Mater*, 1999, **11**, 634-641.
11. C. Galven, J. L. Fourquet, E. Suard, M. P. Crosnier-Lopez and F. Le Berre, *Dalton Trans.*, 2010, **39**, 4191-4197.
12. K. Domen, J. S. T. Yoshimura, A. Tanaka and T. Onishi, *Catal. Lett.*, 1990, **4**, 339.
13. F. Le Berre, M.-P. Crosnier-Lopez, Y. Laligant, E. Suard, O. Bohnke, J. Emery and J.-L. Fourquet, *J. Mater. Chem.*, 2004, **14**, 3558-3565.
14. N. S. P. Bhuvanesh, M.-P. Crosnier-Lopez, H. Duroy and J.-L. Fourquet, *J. Mater. Chem*, 2000, **10**, 1685-1692.
15. Z. Liang, K. Tang, Q. Shao, G. Li, S. Zeng and H. Zheng, *J. Solid State Chem.*, 2008, **181**, 964-970.
16. T. Pagnier, N. Rosman, C. Galven, E. Suard, J. L. Fourquet, F. Le Berre and M. P. Crosnier-Lopez, *J. Solid State Chem.*, 2009, **182**, 317-326.
17. R. Prakash, K. Hunho, C. Yoon-Ho and K. J. Hyun, *ChemElectroChem*, 2018, **5**, 1242-1242.
18. S. J. Fanah, M. Yu, A. Huq and F. Ramezanipour, *J. Mater. Chem. A*, 2018, **6**, 22152–22160.
19. A. C. Larson and R. B. Von Dreele, *General Structure Analysis System (GSAS)*, Los Alamos National Laboratory, 2004.
20. P. Hohenberg and W. Kohn, *Physical Review*, 1964, **136**, B864-B871.
21. W. Kohn and L. J. Sham, *Physical Review*, 1965, **140**, A1133-A1138.
22. G. Kresse and J. Furthmüller, *Physical Review B*, 1996, **54**, 11169-11186.
23. P. E. Blöchl, *Physical Review B*, 1994, **50**, 17953-17979.
24. J. P. Perdew, J. A. Chevary, S. H. Vosko, K. A. Jackson, M. R. Pederson, D. J. Singh and C. Fiolhais, *Physical Review B*, 1992, **46**, 6671-6687.
25. J. P. Perdew, K. Burke and M. Ernzerhof, *Physical Review Letters*, 1996, **77**, 3865-3868.
26. X. Gonze, *Physical Review B*, 1997, **55**, 10337-10354.
27. H. J. Monkhorst and J. D. Pack, *Physical Review B*, 1976, **13**, 5188-5192.
28. B. Toby, *J. Appl. Cryst.*, 2001, **34**, 210-213.

29. B. V. Beznosikov and K. S. Aleksandrov, *Crystallography Reports*, 2000, **45**, 792-798.
30. M.-P. Crosnier-Lopez, F. Le Berre and J.-L. Fourquet, *J. Mater. Chem.*, 2001, **11**, 1146-1151.
31. S. K. Singh and V. R. K. Murthy, *Mater. Res. Bull.*, 2015, **70**, 514-518.
32. M. Ben Bechir, K. Karoui, M. Tabellout, G. Kamel and A. Rhaiem, *Phase Transitions*, 2015, DOI: 10.1080/01411594.2014.987673, 1-17.
33. J. Irvine, D. Sinclair and A. West, *Adv. Mater.*, 1990, **2**, 132-138.
34. J. H. Joshi, D. K. Kanchan, M. J. Joshi, H. O. Jethva and K. D. Parikh, *Materials Research Bulletin*, 2017, **93**, 63-73.
35. J.-F. Wu and X. Guo, *Solid State Ionics*, 2017, **310**, 38-43.
36. O. Bohnke, J. Emery and J.-L. Fourquet, *Solid State Ionics*, 2003, **158**, 119-132.
37. R. Shannon, *Acta Crystallographica Section A*, 1976, **32**, 751-767.
38. V. Thangadurai and W. Weppner, *J. Solid State Chem.*, 2006, **179**, 974-984.
39. V. Thangadurai and W. Weppner, *Ionics*, 2006, **12**, 81-92.
40. S. Roy, S. L. K and K. Uma Rao, *IJMMM* 2014, **2**, 96-100.
41. S. Mulmi, R. K. Hona, J. B. Jasinski and F. Ramezanipour, *J Solid State Electr.*, 2018, DOI: 10.1007/s10008-018-3947-6.
42. N. Murali, S. J. Margarette, V. Kondala Rao and V. Veeraiah, *J. Sci: Adv. Mater. Dev.*, 2017, **2**, 233-244.
43. S. Thakur, R. Rai, I. Bdikin and M. A. Valente, *Materials Research*, 2016, **19**, 1-8.
44. M. R. Biswal, J. Nanda, N. C. Mishra, S. Anwar and A. Mishra, *Advanced Materials Letters*, 2014, **5**, 531-537.
45. C. R. Cena, A. K. Behera and B. Behera, *J. Adv. Cer.*, 2016, **5**, 84-92.
46. A. Arya and A. L. Sharma, *J. Phys. Condens. Matter*, 2018, **30**, 165402.
47. K. L. Gordon, J. H. Kang, C. Park, P. T. Lillehei and J. S. Harrison, *J. Appl. Polym. Sci.*, 2012, **125**, 2977-2985.
48. H. Wang, Y. Chen, D. Hood Zachary, G. Sahu, S. Pandian Amaresh, K. Keum Jong, K. An and C. Liang, *Angewandte Chemie International Edition*, 2016, **55**, 8551-8555.
49. I.-H. Chu, C. S. Kompella, H. Nguyen, Z. Zhu, S. Hy, Z. Deng, Y. S. Meng and S. P. Ong, *Scientific Reports*, 2016, **6**, 33733.
50. Z. Congyan, Y. Ming, A. George, D. Ruchira Ravinath and S. Gamini, *Nanotechnology*, 2017, **28**, 075401.

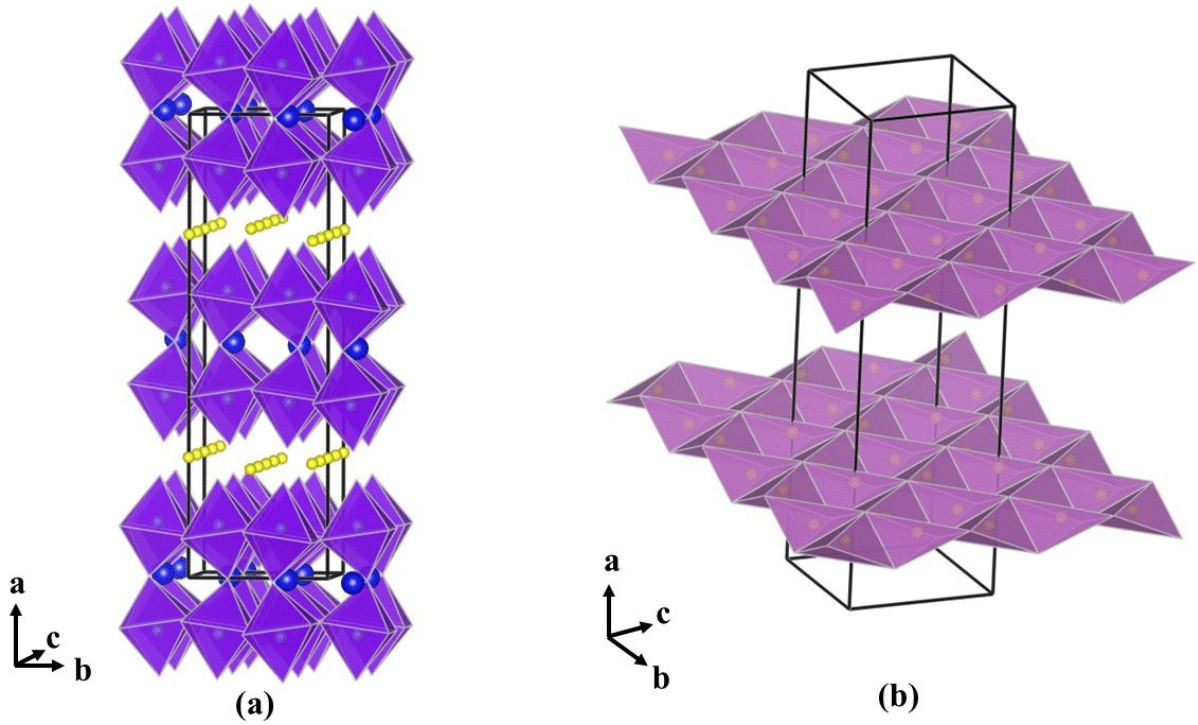

Figure 1. (a) Crystal structure of $Li_2LaNbTiO_7$. Blue, gray and yellow spheres represent La, Nb/Ti, and Li, respectively. **(b)** Tetrahedral coordination environment of lithium.

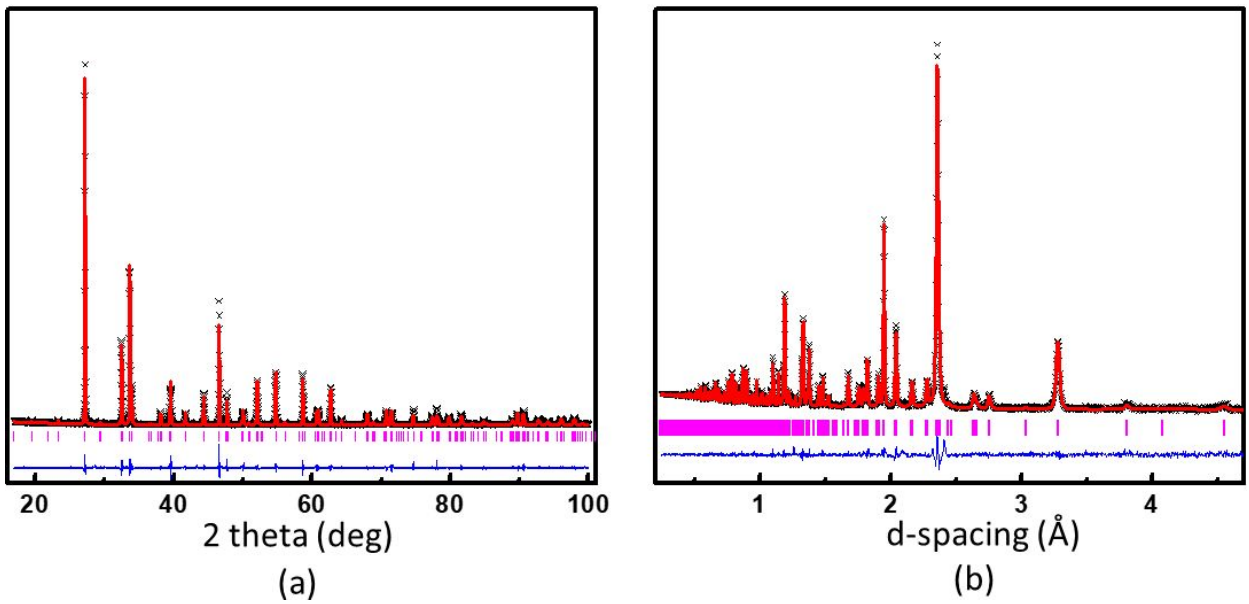

Figure 2. Rietveld refinement profile for $Li_2LaNbTiO_7$ in *Cmcm* space group. **(a)** Powder X-ray diffraction data. **(b)** Neutron diffraction data. The experimental data are represented by black crosses. The red line shows the fit, the vertical tick marks represent Bragg peak positions, and the lower blue line is the difference plot.

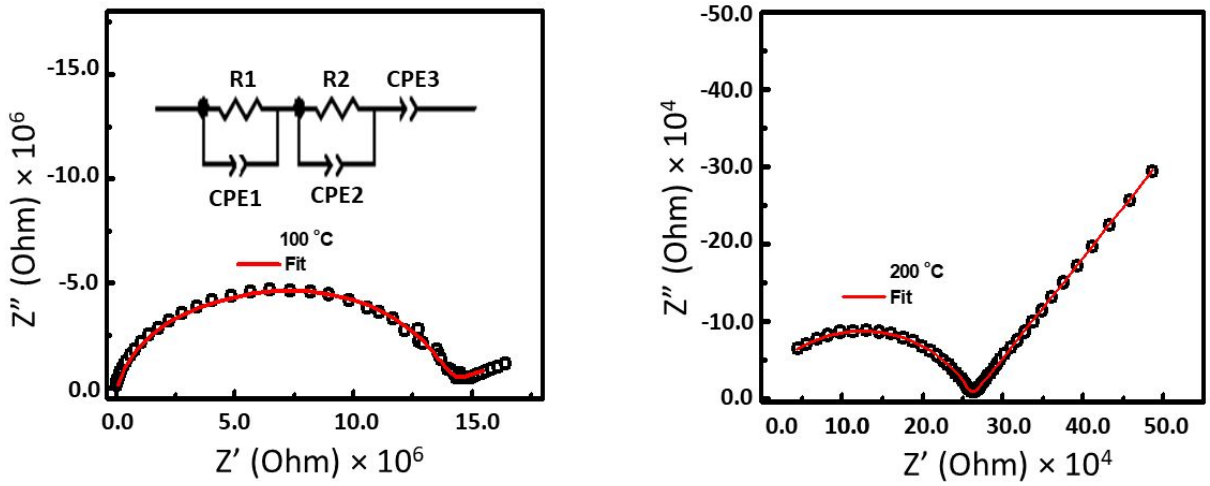

Figure 3. Typical Nyquist Impedance plots for $Li_2LaNbTiO_7$

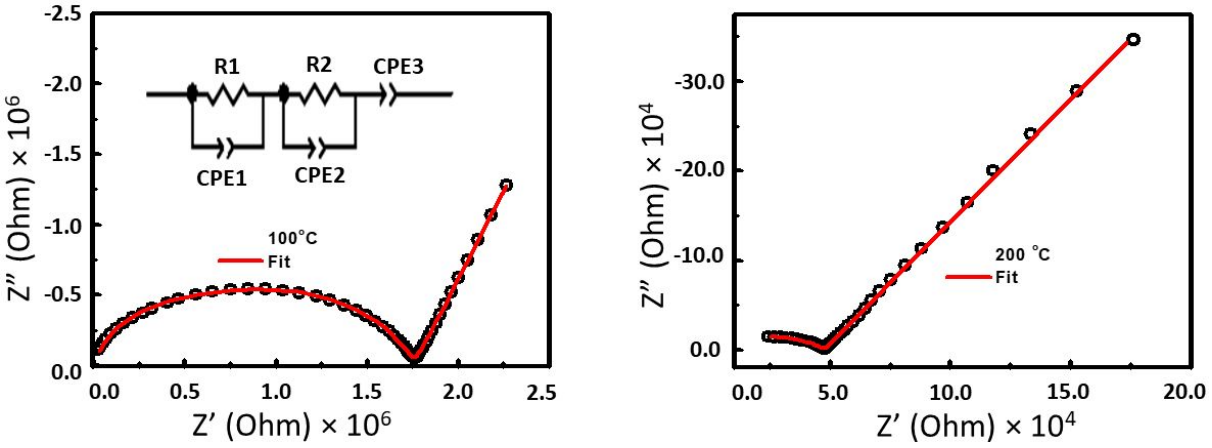

Figure 4. Typical Nyquist Impedance plots for $Li_{1.8}LaNb_{1.2}Ti_{0.8}O_7$

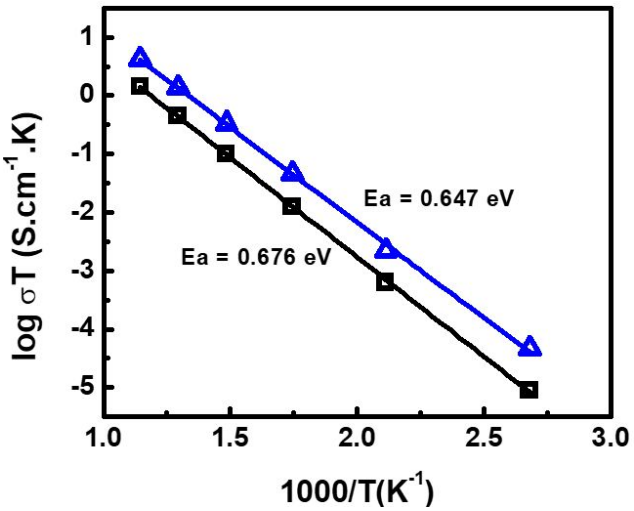

Figure 5. Arrhenius plot for $Li_2LaNbTiO_7$ (black squares) and $Li_{1.8}LaNb_{1.2}Ti_{0.8}O_7$ (blue triangles).

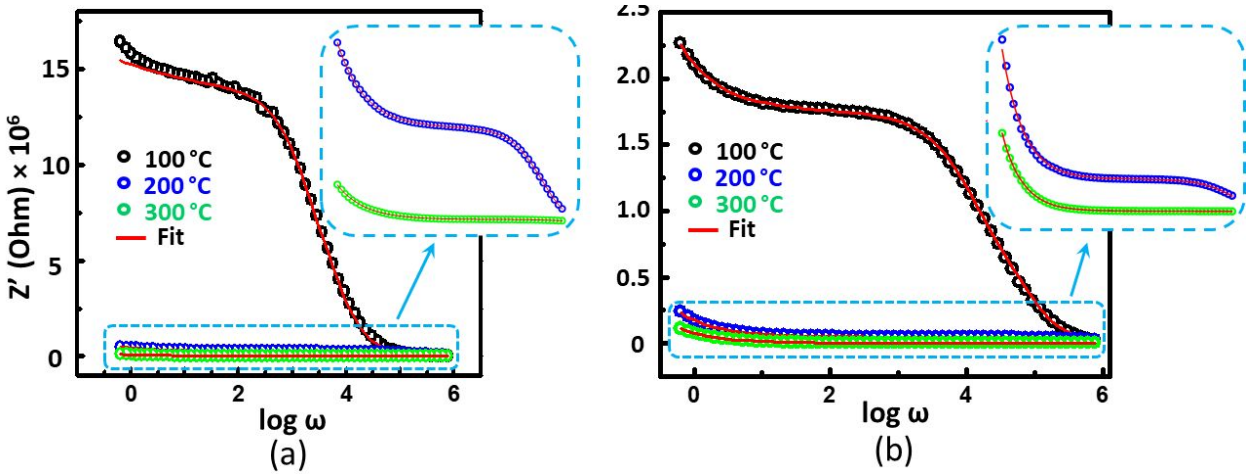

Figure 6. Real part of impedance data as a function of angular frequency (Z' vs log ω) for **(a)** $Li_2LaNbTiO_7$ and **(b)** $Li_{1.8}LaNb_{1.2}Ti_{0.8}O_7$.

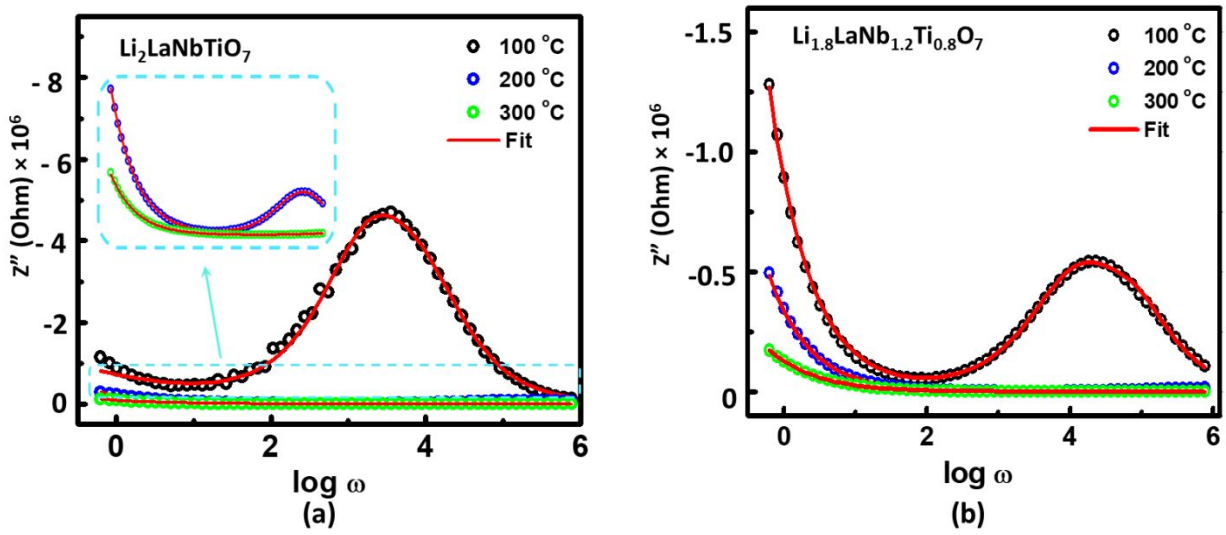

Figure 7. Imaginary part of impedance data as a function of angular frequency (Z'' vs log ω) for $Li_2LaNbTiO_7$ and $Li_{1.8}LaNb_{1.2}Ti_{0.8}O_7$.

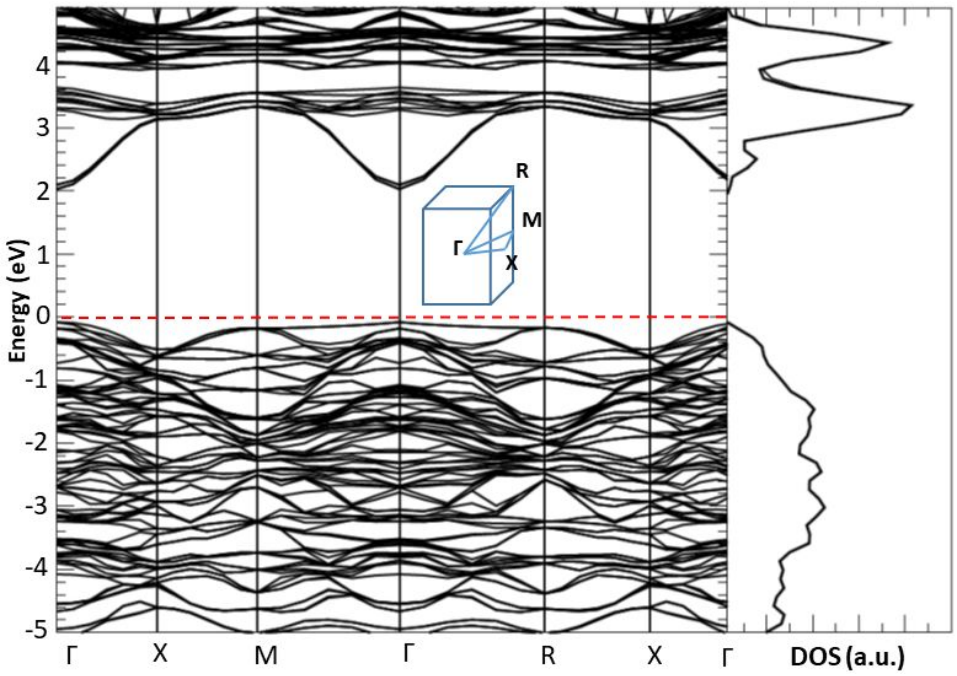

Figure 8. Calculated electronic band structure and density of states (DOS) for $Li_2LaNbTiO_7$. The red dashed line shows the Fermi energy. The Brillouin zone with special high symmetry k points is shown in the inset.

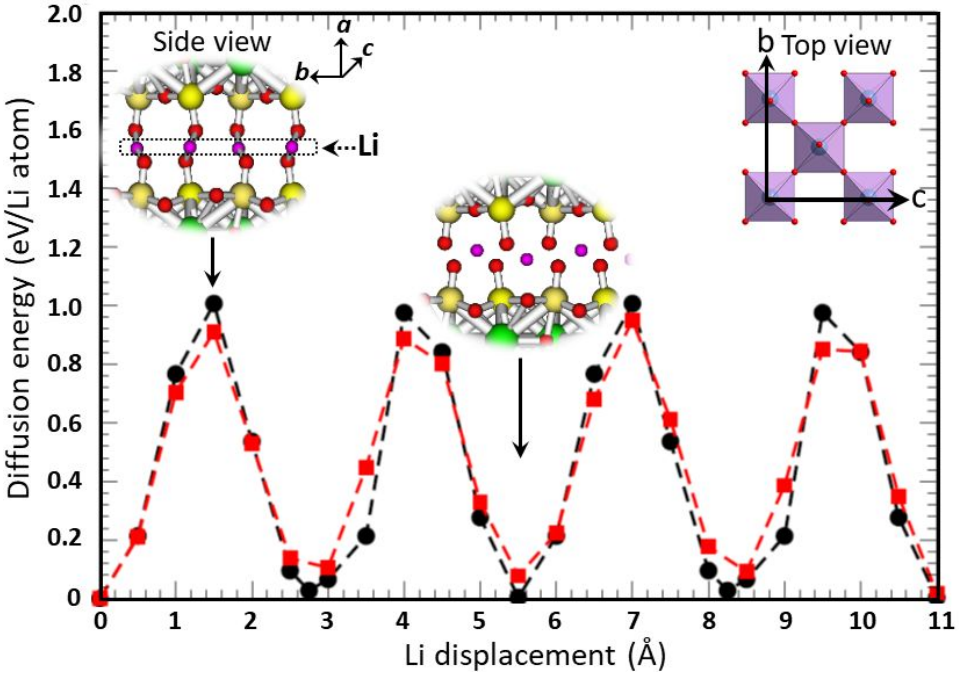

Figure 9. Energy barrier as a function of lithium displacement in *b*-direction for $Li_2LaNbTiO_7$ (black circles) and $Li_{1.8}LaNb_{1.2}Ti_{0.8}O_7$ (red squares). The insets show the structures at the maximum and minimum energies.

Table 1. Structural parameters from Rietveld refinement using neutron diffraction data for $Li_2LaNbTiO_7$. Space group *Cmcm*, $a = 18.2068\ (5)$Å, $b = 5.5150(2)$Å, $c = 5.5040(2)$Å, $Rp = 0.0394$

Atom	x	y	z	Occupancy	U_{iso} (Å^2)	Multiplicity
La1	0	0.2595(4)	0.25	1	0.0052(2)	4
Li1	0.2628(3)	0	0	1	0.0150(7)	8
Nb1	0.1178(2)	0.7509(8)	0.25	0.5	0.00040(3)	8
Ti1	0.1178(2)	0.7509(8)	0.25	0.5	0.00040(3)	8
O1	0	0.6981(4)	0.25	1	0.0108(5)	4
O2	0.2164(9)	0.7804(4)	0.25	1	0.0104(3)	8
O3	0.6114(1)	0	0	1	0.0107(3)	8
O4	0.0911(7)	0	0	1	0.0051(2)	8

Table 2. Structural parameters from Rietveld refinement using X-ray diffraction data for $Li_{1.8}LaNb_{1.2}Ti_{0.8}O_7$. Space group *Cmcm*, a = 18.3608(2) Å, b = 5.51830(1) Å, c = 5.5182(1) Å, *Rp* = 0.888

Atom	x	y	z	Occupancy	U_{iso} (Å^2)	Multiplicity
La1	0	0.2543(10)	0.25	1	0.024(1)	4
Li1	0.2628	0	0	0.9	0.0250	8
Nb1	0.1168(12)	0.7512(10)	0.25	0.6	0.017(1)	8
Ti1	0.1168(12)	0.7512(10)	0.25	0.4	0.0159(8)	8
O1	0	0.750(9)	0.25	1	0.018(8)	4
O2	0.2147(6)	0.769(5)	0.25	1	0.029(5)	8
O3	0.6060(17)	0	0	1	0.09(1)	8
O4	0.0955(12)	0	0	1	0.003(6)	8

Table 3. Variable temperature conductivity of $Li_2LaNbTiO_7$ and $Li_{1.8}LaNb_{1.2}Ti_{0.8}O_7$

	Conductivity (S cm^{-1})	
Temperature (ºC)	**$Li_2LaNbTiO_7$**	**$Li_{1.8}LaNbTa_{1.2}Ti_{0.8}O_7$**
25	N/A	4.258×10^{-9}
100	2.360×10^{-8}	1.241×10^{-7}
200	1.310×10^{-6}	4.584×10^{-6}
300	2.150×10^{-5}	8.063×10^{-5}
400	1.450×10^{-4}	4.960×10^{-4}
500	5.731×10^{-4}	1.780×10^{-3}
600	1.626×10^{-3}	4.713×10^{-3}